Effect of Trap-assisted Tunneling (TAT) on the Performance of Homojunction Mid-Infrared Photodetectors based on InAsSb

P. Chakrabarti, A. Gawarikar, V. Mehta, and D. Garg

Centre for Research in Microelectronics, Department of Electronics Engineering, Institute of Technology, Banaras Hindu University
Varanasi – 221005, INDIA
e-mail: pchakra@bhu.ac.in

ABSTRACT

Theoretical investigations have been carried out to explore the effect of trap-assisted tunneling on the performance characteristics of an InAsSb p^+–n homojunction photodetector supposed to be grown on InAs substrate. Both electrical and optical characterizations of the device have been simulated for operation of the device in the mid-infrared region (2.5-4.0 μm). The study revealed that the dark current of the photodetector under reverse bias is dominated by trap-assisted tunneling component of current and this causes the detectivity of the device to decrease at high reverse bias. It was concluded that by operating the device at a suitable low reverse bias it is possible to improve the room-temperature detectivity significantly as compared to its value at zero bias.

Index Terms: Detectivity, InAs/InAsSb, mid-infrared (MIR), photodetector, trap-assisted tunneling (TAT), band-to-band tunneling (BTB), and resistance area product.

1. INTRODUCTION

The absorption bands of a number of combustible and atmospheric pollutant gases are contained in the mid-infrared (2-5μm) spectral range. Portable gas sensors deploy mid-infrared semiconductor detectors that are low-cost and reliable. A large number of semiconductor detectors have been developed over the past decades for application in the mid-infrared (MIR) region [1]-[8]. Currently the dominant mid-infrared detector materials include IV-VI and II-VI alloys such as PbSe, HgCdTe and III-V alloys such as InSb and its related ternary and quaternary alloys. Because of some inherent difficulties with IV-VI and II-VI materials [9], the $InAs_{1-x}Sb_x$ ternary III-V alloy eventually emerged as potentially more promising for application in the mid-infrared region. The detectors based on $InAs_{1-x}Sb_x$ however, require cryogenic cooling to 77K in order to obtain a high value of detectivity. This highly restricts the use of these devices in portable gas sensing equipment. It is therefore, necessary to develop efficient and reliable MIR photodetectors that can work at room temperature. A major constraint in the development of $InAs_{1-x}Sb_x$ detectors is the preparation of high quality epitaxial layers of desired concentration on InAs substrate. The interface

quality can be improved significantly by restricting the value x (<0.05). In this present paper we describe a theoretical model for characterization of an LPE grown p^+-n^0 $InAs_{0.96}Sb_{0.04}$ detector on InAs (100) substrate. The present work aims at exploring the role of various components of dark current on the electrical and optical characteristics of a homojunction p^+-n^0 $InAs_{0.96}Sb_{0.04}$ photodetector proposed to be grown on InAs substrate. Emphasis has been given on the investigation of the effect of tunneling via traps and dependence of the resistance-area product of the device on the location of the trap level inside the energy bandgap.

2. DEVICE STRUCTURE AND MODELING OF DARK CURRENT COMPONENTS

The structure under consideration is a homojunction p^+-n^0 $InAs_{0.96}Sb_{0.04}$ photodiode supposed to be grown on an InAs (100) substrate. A schematic of the structure is shown in Fig.1a and the energy band diagram illustrating the transport of photogenerated carriers across the junction in Fig.1b. The top p^+ layer receives the incident light and the lightly doped n^0 region acts as the active layer. The incident light is absorbed in the neutral p^+, n^0 regions as well as in the space charge region formed at the p^+-n^0 junction. The carriers generated in the neutral p^+ and n^0 regions beyond their respective diffusion lengths would recombine before reaching the junction and fail to contribute to the net photocurrent. The dark current of the InAsSb photodetector has been modeled here by considering (i)the diffusion of the thermally generated carriers from the neutral regions, I_{DIFF} ; (ii)generation-recombination of carriers in the depletion region, I_{GR} and (iii)tunneling of carriers through the barrier, I_{TUN}. In order to generalize the analysis, we have however considered both trap assisted tunneling (TAT) as well as band-to-band tunneling (BTB). The tunneling component of current thus constitutes two components e.g., I_{TAT} arising from the trap assisted tunneling and I_{BTB} arising out of band-to-band tunneling. The net current can be written as

$$I = I_{DIFF} + I_{GR} + I_{TAT} + I_{BTB} \tag{1}$$

Ohmic component of current and contribution due avalanche multiplication are ignored in the present model.

In this section the relevant expressions for calculating the dark currents and the associated dynamic impedance contribution due to each of these mechanisms are outlined.

2.1 Diffusion component

In the present structure the diffusion component of current would be dominated by the holes injected from p^+ region into the n^0 region. The minority carrier diffusion current density under application of a bias voltage, V can be approximated as [10]

$$J_{DIFF} = C\frac{qn_i^2}{N_d}\left[\frac{kT}{q}\frac{\mu_p}{\tau_{eff}}\right]^{\frac{1}{2}}\left(\exp\left(\frac{qV}{kT}\right)-1\right) \tag{2}$$

where N_d is the donor concentration in the n^0 region, n_i is the intrinsic carrier concentration, τ_{eff} is the effective lifetime of minority carriers in the n^0 active region, μ_p is the mobility of holes. The factor C accounts for the surface recombination velocity at the InAs/InAsSb interface of the active n^0 region of thickness, d given by

$$C = \frac{\frac{S_p L_p}{D_p}\cosh\left(\frac{d-x_n}{L_p}\right)+\sinh\left(\frac{d-x_n}{L_p}\right)}{\frac{S_p L_p}{D_p}\sinh\left(\frac{d-x_n}{L_p}\right)+\cosh\left(\frac{d-x_n}{L_p}\right)} \tag{3}$$

where L_p is the hole diffusion length in the n^0 region and S_p is the surface recombination velocity of holes at InAs/InAsSb interface on n^0 side.

The product of dynamic resistance and area (RA) is given by the reciprocal of the derivative of the current density with respect to voltage. The diffusion component of RA product can be obtained as

$$\frac{1}{(RA)_{DIFF}} = \frac{dJ_{DIFF}}{dV} = \frac{Cq^2 n_i^2}{kTN_d}\left\{\frac{kT\mu_p}{q\tau_{eff}}\right\}^{1/2}\exp\left(\frac{qV}{kT}\right) \tag{4}$$

where μ_p is the mobility of holes in the n^0 region.

2.2 Generation-recombination current

Generation-recombination (GR) component of current is due to defects within the depletion region which act as intermediate states for the thermal generation and recombination of carriers. These intermediate states are referred to as Shockley Read centres. The generation-recombination component of current density can be approximated as [11]

$$J_{GR} = \frac{qn_i WV}{(V_{bi}-V)\tau_{SRH}} \quad \text{for } V<0 \tag{5a}$$

and

$$J_{GR} = \frac{2n_i WkT}{(V_{bi}-V)\tau_{SRH}}\sinh\left(\frac{qV}{2kT}\right) \quad \text{for } V>0 \tag{5b}$$

where V_{bi} is the built-in potential, V is the applied voltage, W is the width of the depletion region which is a function of the applied voltage and n_i is the intrinsic carrier concentration and τ_{SRH} is the SRH generation-recombination lifetime.

The associated resistance-area product in the two cases can be obtained as

$$\left.\frac{1}{(RA)_{GR}}\right|_{V<0} = \left(\frac{dJ_{GR}}{dV}\right)_{V<0}$$

$$= \frac{qn_i}{\tau_{SRH}}\left(\frac{2\varepsilon_s(N_a+N_d)}{qN_aN_d}\right)^{\frac{1}{2}}\left(\frac{1}{(V_{bi}-V)^{\frac{1}{2}}}+\frac{V}{2(V_{bi}-V)^{\frac{3}{2}}}\right) \tag{6a}$$

$$\left.\frac{1}{(RA)_{GR}}\right|_{V>0} = \left(\frac{dJ_{GR}}{dV}\right)_{V>0}$$

$$= \frac{qn_i}{\tau_{SRH}}\left(\frac{2\varepsilon_s(N_a+N_d)}{qN_aN_d}\right)^{\frac{1}{2}}\left(\frac{kT}{q(V_{bi}-V)^{\frac{3}{2}}}\sinh\left(\frac{qV}{2kT}\right)+\frac{1}{(V_{bi}-V)^{\frac{1}{2}}}\cosh\left(\frac{qV}{2kT}\right)\right) \tag{6b}$$

where ε_s is the dielectric constant.

2.3 Trap-assisted tunneling

Trap-assisted tunneling occurs when minority carriers tunnel from occupied trap states on the quasi-neutral side to the empty band states on the other side of the junction or though trap sites present in the depletion region of the junction. This mechanism is shown in the energy band diagram of Fig.1 (b). These trap centers are intermediate energy levels created by the presence of impurities in the material. The trap-assisted tunneling component of current density calculated on the basis of simple one-dimensional model [10] can be written as

$$J_{TAT} = \frac{q^3 m_n^* E M^2 W N_T}{8\pi\hbar^3 (E_g - E_T)} \exp\left(- \frac{4\sqrt{2m_n^* (E_g - E_T)^3}}{3q\hbar E} \right) \tag{7}$$

where E_g is the energy bandgap of the semiconductor, $\hbar = h/2\pi$; h being the Planck's constant, E is the maximum electric field across the depletion region, E_T is energy (in eV) corresponding to trap centres, measured from top of the valence band, m_n^* is the effective mass of electrons in the conduction band, N_T is the density of traps occupied by electrons. M is the matrix element associated with the trap potential [10]. The resistance area product associated with trap-assisted tunneling can be obtained as

$$\frac{1}{(RA)_{TAT}} = \frac{dJ_{TAT}}{dV}$$

$$= \frac{2q^3 m_n^* M^2 N_T}{8\pi\hbar^3 (E_g - E_T)} \exp\left(- \frac{B}{\sqrt{(V_{bi} - V)}} \right) \left(1 + \frac{B}{2\sqrt{(V_{bi} - V)}} \right) \tag{8}$$

where $B = \dfrac{-4\sqrt{2m_n^* (E_g - E_T)^3}}{3q\hbar\sqrt{(2qN_a / \varepsilon_0 \varepsilon_s)}}$

2.4 Band-to-band tunneling

At high reverse bias voltages, the crossover of energy bands takes place and electrons directly tunnel from the valence band on the p+ side to the conduction band on the n side. This phenomenon is responsible for the flow of band-to-band tunneling current. The band-to-band tunneling component of current density can be obtained in the closed form as [12]

$$J_{BTB} = \frac{\sqrt{2m_n^*} q^3 E V}{4\pi^2 \hbar^2 E_g^{1/2}} \exp\left(- \frac{4\sqrt{2m_n^*} E_g^{3/2}}{3qE\hbar} \right) \tag{9}$$

The corresponding resistance area product can be obtained by differentiating equation (9) with respect to V and taking the reciprocal. The band-to-band tunneling component of RA product can be obtained as

$$\frac{1}{(RA)_{BTB}} = \frac{q^3}{4\pi^2\hbar^2} \sqrt{\frac{2m_n^*}{E_g}} \exp\left(- \frac{4\sqrt{2m_n^*} E_g^{3/2}}{3q\hbar} \right) \left(E + \frac{V}{2(V_{bi} - V)} \left(E + \frac{4\sqrt{2m_n^*} E_g^{3/2}}{3q\hbar} \right) \right) \tag{10}$$

Considering the effect of all the four mechanisms discussed above, the net value of the resistance-area product can be written as

$$\frac{1}{(RA)_{NET}} = \frac{1}{(RA)_{DIFF}} + \frac{1}{(RA)_{GR}} + \frac{1}{(RA)_{TAT}} + \frac{1}{(RA)_{BTB}} \tag{11}$$

2.5 Lifetime modeling

In order to compute the drift and diffusion components of current accurately, it is necessary to model the lifetime of minority carriers considering all the possible recombination mechanisms. In the analysis, we have taken into account all the three dominant recombination processes e.g., band-to-band radiative recombination, and non-radiative Auger and Shockley-Read-Hall (SRH) recombination mechanisms.

The modeling of the radiative recombination process is straightforward. For direct bandgap semiconductors, the lifetime of carriers due to radiative recombination can be written as

$$\tau_{RAD} = \frac{1}{B_r(n_0 + p_0)} \tag{12}$$

where B_r is the radiative recombination coefficient of the material and n_0 and p_0 are the electron and hole concentrations in the region under thermal equilibrium.

On the other hand the non-radiative Auger recombination is quite complex. In a semiconductor with a single conduction band and heavy-hole and light-hole valence band there can be atleast ten different types of Auger transitions. Out of these transitions, the two most significant transitions that occur at the minimum threshold energy (E_T=E_g) are the Auger-1 or CHCC (involving two conduction band electrons and a heavy hole) and Auger-7 or CHLH (involving one conduction band electron and one heavy hole and one light hole). The former is generally dominant in n-type material and the later in p-type material. In the present analysis we have assumed that InAsSb has a band structure similar to that of InSb. For InSb like band structures in which the spin split-off energy approaches the bandgap of the material, another type of Auger transition that occurs through one conduction band electron, one heavy hole and one spin split-off band hole also becomes significant. This type of Auger process is known as Auger-S or CHSH process. The spin-split off band energy for the material under consideration ($InAs_{0.96}Sb_{0.04}$) has been estimated to be 0.37 eV, which is comparable to the bandgap energy of the material of 0.32 eV at room temperature. In our model we have therefore, considered the effect Auger-S recombination process for computation of the effective lifetime of the carriers. The net Auger recombination lifetime of the carriers can thus be written as [1]

$$\frac{1}{\tau_{AU}} = \frac{1}{\tau_{A-1}} + \frac{1}{\tau_{A-7}} + \frac{1}{\tau_{A-S}} \tag{13}$$

where τ_{AU} corresponds to the overall value of the mean lifetime of the carriers due to Auger recombination and the other suffixes indicate the components of τ for the corresponding Auger transitions. The details of computation of the various components of Auger recombination lifetime is discussed in details elsewhere [6].

The lifetime of carriers due to Shockley-Read-Hall recombination can be modeled in terms of trap density and capture cross-section as

$$\tau_{SRH} = \frac{1}{\sigma N_f v_{th}} \tag{14}$$

where N_f is the SRH trap density, σ is the capture cross-section and v_{th} is the thermal velocity of the minority carriers in the active region, given by

$$v_{th} = \sqrt{\frac{3kT}{m_p^*}} \tag{15}$$

m_p^* is the effective mass of holes in the active region.

The effective lifetime of the carriers in the active region can be obtained as

$$\frac{1}{\tau_{eff}} = \frac{1}{\tau_{RAD}} + \frac{1}{\tau_{AU}} + \frac{1}{\tau_{SRH}} \tag{16}$$

2.6 Specific Detectivity

The most important figure of merit of the MIR photodetector for use in non-telecommunication application is the specific detectivity D^*, which depends on the wavelength of incident light λ, the quantum efficiency η and the zero-bias resistance-area product, R_0A. As the dark current of the detector is contributed by three major components e.g., diffusion, generation-recombination and tunneling which includes trap assisted tunneling (TAT) as well as band-to-band (BTB) tunneling, the detectivity of the photodetector under consideration should be estimated from the net value of the R_0A product arising out of these mechanisms. The specific detectivity of the photodetector which is a function of the applied voltage can be written as

$$D^* = \frac{q\eta\lambda}{hc}\sqrt{\frac{(RA)_{NET}}{4kT}} \tag{17}$$

where, η is the quantum efficiency, λ is the operating wavelength and $(RA)_{NET}$ is the net or effective value of the resistance area product which is a function of the applied voltage.

The quantum efficiency (η) of a p-n junction photodetector has generally three major components. These components arise from the contribution of the three regions e.g., neutral n-region (η_n), neutral p-region (η_p) and the depletion region (η_{dep}). The optical generation rate of electron-hole pairs, as a function of distance x from the surface can be written as

$$G(x) = \frac{\alpha(\lambda)(1-R)P_{op}}{Ah\nu}\exp(-\alpha(\lambda)x) \tag{18}$$

where α(λ) is the optical absorption coefficient of the material which is a function of wavelength λ, r is the Fresnel reflection coefficient at the entrance, P_{op} is the incident optical power, ν is the frequency of radiation and A is the device area. The quantum efficiency components can be obtained as [4]

$$\eta_n = \frac{(1-R)\,\alpha L_p}{\alpha^2 L_p^2 - 1}\exp(-\alpha(t+x_n))\left[\frac{(\gamma_p - \alpha L_p)\exp(-\alpha(d-x_n)) - \left[\gamma_p \cosh\left(\frac{d-x_n}{L_p}\right) + \sinh\left(\frac{d-x_n}{L_p}\right)\right]}{\gamma_h \sinh\left(\frac{d-x_n}{L_p}\right) + \cosh\left(\frac{d-x_n}{L_p}\right)} + \alpha L_p\right] \tag{19}$$

$$\eta_p = \frac{(1-R)\,\alpha L_n}{\alpha^2 L_n^2 - 1}\left[\frac{\alpha L_n + \gamma_n - \exp(-\alpha(t-x_p))\left[\gamma_n \cosh\left(\frac{t-x_p}{L_n}\right) + \sinh\left(\frac{t-x_p}{L_n}\right)\right]}{\gamma_n \sinh\left(\frac{t-x_p}{L_n}\right) + \cosh\left(\frac{t-x_p}{L_n}\right)} - \alpha L_n \exp(-\alpha(t-x_p))\right] \tag{20}$$

where L_p and L_n are the hole and electron diffusion lengths in n^0 and p^+ regions respectively. $\gamma_n = S_n L_n / D_n$ and $\gamma_p = S_p L_p / D_p$ are the ratio of surface to bulk recombination velocity in p^+ and n^0 regions respectively.

The contribution of the photo-generated carriers in the depletion region to the total quantum efficiency can be obtained as

$$\eta_{dep} = (1-R)\{\exp(-\alpha(t-x_p)) - \exp(-\alpha(t+x_n))\} \quad (21)$$

The net quantum efficiency can be written as

$$\eta = \eta_n + \eta_p + \eta_{dep} \quad (22)$$

3. RESULTS AND DISCUSSION

Numerical computations have been carried out on p^+-$InAs_{0.96}Sb_{0.04}$/n^0-$InAs_{0.96}Sb_{0.04}$/n^+- $InAs_{0.96}Sb_{0.04}$ photodetector at 300 K. The light has been assumed to be incident from the top p^+- $InAs_{0.96}Sb_{0.04}$ side. The incident photons with energy higher than the band gap of $InAs_{0.96}Sb_{0.04}$ are absorbed in both p^+ and n^0 regions. Various parameters used in the theoretical computations are taken from references [13]-[14] and are listed in Table-1. The absorption coefficient of InAsSb has been computed as a function of wavelength by following Anderson's formula [15] and incorporating Moss-Burstein shift. In the computation, the matrix element M^2 used in equation (8) has been assumed to 10^{-29} V^2 m^3 which is reasonable for acceptor-type traps in the Zinc-blende lattice as experimentally determined by others [10].

The different components of the dark current and the RA products have been calculated using the theoretical model discussed in the previous section. The dependence of the RA product on the applied voltage has also been estimated quantitatively. The variation of the theoretically estimated detectivity of the detector at room temperature with the wavelength of operation has also been computed.

TABLE 1. Device parameters used in the computation.

Parameters	Values
E_g	$0.411 - \frac{3.4\times10^{-4}T^2}{T+210} - 0.876x + 0.7x^2 + 3.4\times10^{-4}x(1-x)T$ eV
N_T	10^{17} /m^3
N_d	10^{22} /m^3
N_a	10^{24} /m^3
m_n^*	m_o (0.023 - 0.039x + 0.03x^2)
m_p^*	m_o (0.41 + 0.02x)
A	3.14 x 10^{-8} m^2
ε_s	(15.15 + 1.65x) ε_0
M^2	10^{-29} V^2m^3
S_n	1000 m/s
S_p	10 m/s

Fig.2 shows the variation of the components of current density arising from the diffusion, generation-recombination and tunneling (trap-assisted and band-to-band) with the applied reverse bias voltage along with the variation of the net current density. In the reverse direction the tunneling component of current is found to play an important role in deciding the total reverse saturation current. Results of numerical computation reveal that the trap assisted tunneling component is dominant even at low reverse voltage while the band-to-

band tunneling becomes significant only at a very high reverse voltage. The actual nature of the current voltage characteristic of the detector is largely dependent on the processing history of the device. In devices fabricated with a large number of traps, the reverse saturation current does not remain constant and independent of reverse voltage. This nature is attributed to trap-assisted tunneling that occurs via the defects in the device. The contribution of the trap-assisted tunneling component however, depends on the number of trap centres as well as the location of the trap level inside the forbidden energy gap.

The variation of the net current with reverse voltage for a fixed value N_T ($=10^{17}/m^3$) is shown in Fig.3 for different positions of the trap levels measured as E_T in eV from the valence band-edge within the forbidden energy bandgap. It is seen that when the trap level is very close to the valence band-edge (small E_T arising primarily from shallow doping) the reverse saturation current remains nearly constant even at large reverse voltage. On the other hand as the position of the trap level moves towards the middle of the bandgap, the reverse saturation current increases very fast as the applied reverse voltage increases beyond a threshold value.

Fig.4 shows the variations of the resistance-area product of the detector arising from various components (diffusion, generation-recombination, trap-assisted and band-to-band tunneling components as well as their net value with the applied reverse bias voltage. At a low reverse voltage the RA product due to both the tunneling components are very high because of negligible flow of tunneling current at such a low reverse voltage. The overall RA product of the detector is mainly decided by the diffusion and generation-recombination components. However, as the reverse bias voltage increases, the trap-assisted tunneling component of RA becomes significantly low (less than both the diffusion and generation-recombination components) and the overall RA product of the detector is dictated by the trap-assisted tunneling component. The effect of band-to-band tunneling remains almost negligible. At a low reverse voltage all the three mechanisms are found to be competitive. The net effect is a peaking of the RA versus voltage curve. The reverse voltage at which the peak occurs depends on the values of E_T and relative contribution of the diffusion and generation-recombination components. The magnitude of the peak depends on various material parameters and device dimensions.

The effect of the position of E_T on the variation of RA product with voltage is depicted in Fig.5. In this case N_T has been assumed to be 10^{17} /m^3 and the product of $N_f\sigma$ has been assumed to be 10 m^{-1}. The later parameter decides the SRH recombination lifetime and affects the generation-recombination component significantly. It is observed that when the trap centre creates an energy level far away from the band-edge, the RA product has a peak which occurs at a low reverse voltage and the product drops significantly under zero-bias condition. The RA product and hence the detectivity of the detector in such cases can be improved by operating the device under a small reverse bias rather than at zero bias.

The effect of generation-recombination component of the dark current on the net RA product is shown in Fig.6. This figure depicts the variation of the net RA product with the applied reverse voltage for different values of SRH trap density and capture cross-section product ($N_f\sigma$). In this computation the trap density responsible for trap-assisted tunneling has been assumed to be $10^{17}/m^3$ and position of the trap centre from the valence band edge has been assumed to be 0.08 eV. It can be easily seen that the shape of the RA versus voltage curve depends on the SRH recombination. In other words, both SRH and TAT components would primarily shape the variation of resistance-area product versus voltage of the device with in the low and moderate reverse bias region.

The variation of specific detectivity of the detector at room temperature is shown in Fig.7 as a function of the operating wavelength. It is seen that the homojunction p^+-$InAs_{0.96}Sb_{0.04}/n^0$-$InAs_{0.96}Sb_{0.04}/n^+$-$InAs_{0.96}Sb_{0.04}$ photodetector under consideration exhibits a

peak detectivity of 7.48 $\times 10^8$ mHz$^{1/2}$/W at λ=3.09 μm. The detectivity falls very fast beyond the long wavelength cut-off. At shorter wavelength the detectivity falls rather slowly. Computations reveal (not shown here) that while a wider active region improves the detectivity of the device, a thicker cladding region may significantly reduce the detectivity in the shorter wavelength region. This effect is however more pronounced in heterojunction photodetectors reported earlier [6]. The variation of the detectivity with wavelength for different composition of the material is also illustrated in this figure. As the present device is supposed to be grown on InAs substrate, the mole fraction of Sb has been restricted to 4% so that the lattice mismatch at InAs/InAsSb interface is not very large. For longer wavelength operation $InAs_{1-x}$ Sb_x (x>0.04) may be grown on a GaSb substrate to have a better interface quality.

4. CONCLUSION

In this paper the effect of the trap-assisted tunneling on the detectivity of a homojunction p^+-n photodetector based on InAsSb has been explored theoretically. The study reveals that the performance of an InAsSb based homojunction photodetector is restricted by the trap-assisted tunneling component of dark current. Further, the resistance-area product of the detector and hence its detectivity can be improved significantly (more than an order of 10) by operating the device at a suitable reverse voltage. The model presented here can be used by design engineers as a tool for detecting the presence of trap centre in the processed device. The model can also be used for optimization purposes, which in turn will reduce the number of experimental trials required for the development of improved photodetectors.

REFERENCES

1. A. Rogalski, K. Adamiec and J. Rutkowski: 'Narrow-Gap Semiconductor Photodiode', SPIE Press, Bellingham, USA, 2000.
2. A. Rogalski, "New trends in semiconductor infrared detectors," Opt. Engg., **33**, pp.1395-1412, 1994.
3. A. Krier, H.H. Gao, V.V. Sherstnev: 'Room temperature $InAs_{0.89}$ $Sb_{0.11}$ photodetectors for CO detection at 4.6 μm', *Applied Phys. Lett*., **77,** (6), pp. 872- 874, 2000.
4. Y. Tian, B. Zhang, T. Zhan, H. Jiang, Y. Jin: 'Theoretical analysis of the detectivity in N-p and P-n GaSb/GaInAsSb infrared photo-Detectors', *IEEE Trans. Electron Dev*., **ED-47**, pp. 544-551, 2000.
5. X.Y. Gong, T. Yamaguchi, H. Kan, T. Makino, T. Iida, T. Kato, M. Aoyama, Y. Hayakama, and M. Kumagawa : 'Room temperature InAsx$P_{1-x-y}Sb_y$/InAs photodetectors with large quantum efficiency'*, Jpn. J. Appl. Phys*., **36**, pp. 2614-2616, 1997.
6. P. Chakrabarti, A. Krier, and A. F. Morgan, "Analysis and Simulation of a Mid-Infrared P^+-$InAs_{0.55}Sb_{0.15}P_{0.30}$/$n^0$-$InAs_{0.89}Sb_{0.11}$/$N^+$-$InAs_{0.55}Sb_{0.15}P_{0.30}$ Double Heterojunction Photodetector Grown by LPE," IEEE Trans. on Electron Devices, **50**, 2003
7. A. Rogalski, "Heterostructure infrared photovoltaic detectors," Infrared Physics and Technology, **41**, pp.213-238, 2000.
8. A. Rogalski, R. Ciupa, W. Larkowski, "Near room temperature InAsSb photodiodes: theoretical predictions and experimental data," Solid-state Electronics, vol.39, pp.1593-1600, 1996.
9. N.T. Niedziela and R. Ciupa, "Ultimate parameters of $Hg_{1-x}Cd_xTe$ and $InAs_{1-x}Sb_x$ n^+-p photodiodes," Solid-state Electronics, **45**, pp41-46, 2001.

10. V.Gopal, S.K. Singh and R.M. Mehra, 'Analysis of dark current contributions in mercury cadmium telluride junction diodes', *Infrared Physics and Technology*, **43**, pp.317-326, 2002.
11. R. Schoolar, S Price, J Rosbeck, "Investigation of the generation–recombination currents in HgCdTe midwavelength infrared photodiodes," J. of Vacuum Science and Tech. B, **10**, pp.1507-1514, 1992.
12. S.M. Sze, "Physics of Semiconductor Devices," Wiley Eastern Ltd., New Delhi, 1981.
13. M. Levinshtein, S. Rumyantsev, and M. Shur: "Hand book series on Semiconductor Parameters," **1**, World Scientific, 1996.
14. M. Levinshtein, S. Rumyantsev and M.S. Shur: "Hand book series on Semiconductor Parameters," **2**, World Scientific, 1996.
15. W.W. Anderson: 'Absorption constant of $Pb_{1-x}Sn_xTe$ and $Hg_{1-x}Cd_xTe$ alloys', *Infrared Physics*, **20**, pp.363-372, 1980.

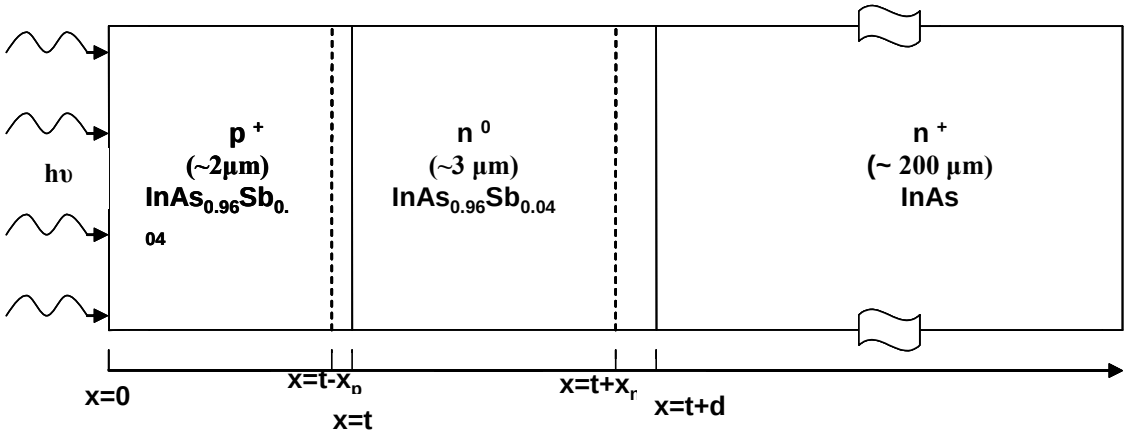

Fig.1a. Schematic diagram of the device structure.

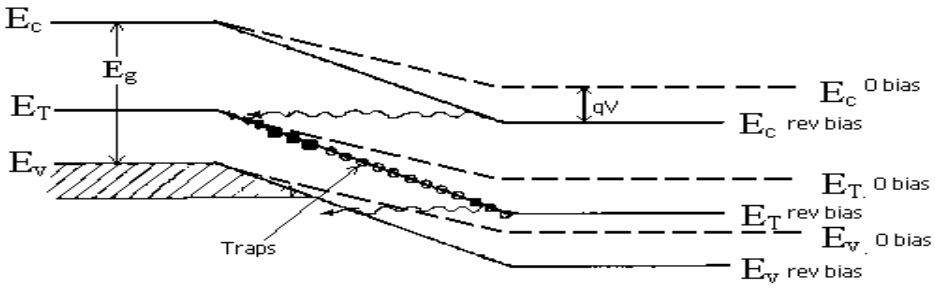

Fig. 1b. Energy band diagram showing band-to-band and trap-assisted tunneling components.

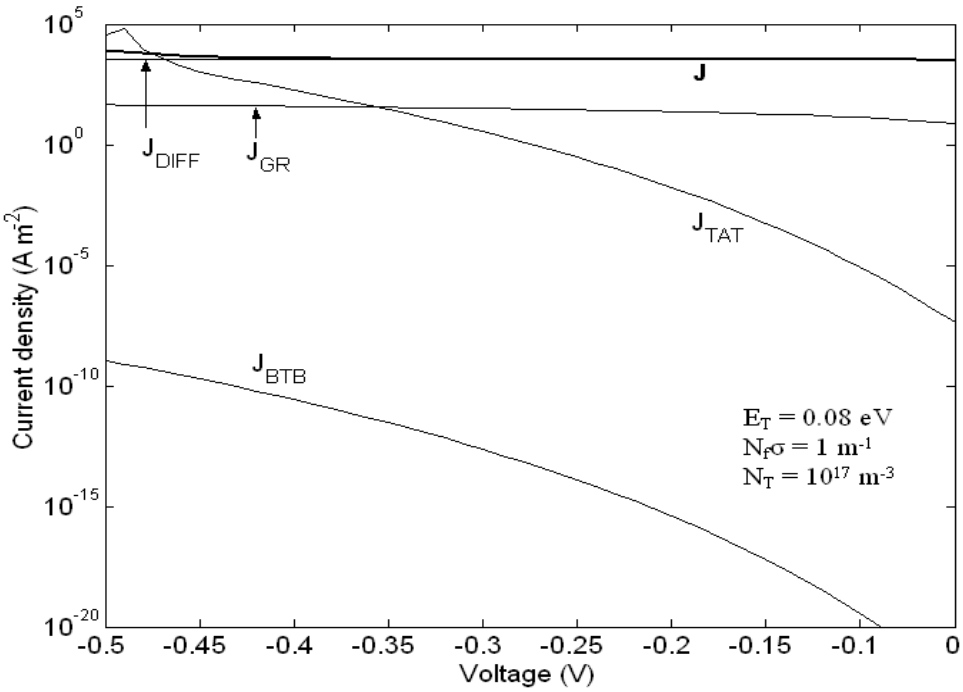

Fig. 2. Variation of different components of dark current density with applied reverse voltage.

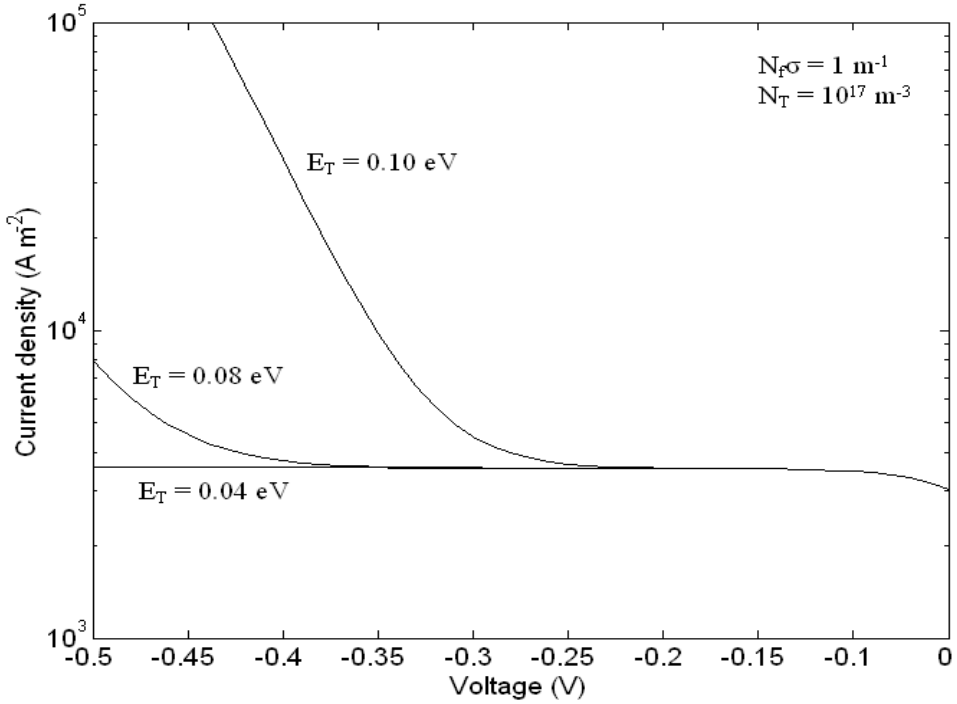

Fig. 3. Effect of E_T on the variation of total current density with applied reverse voltage.

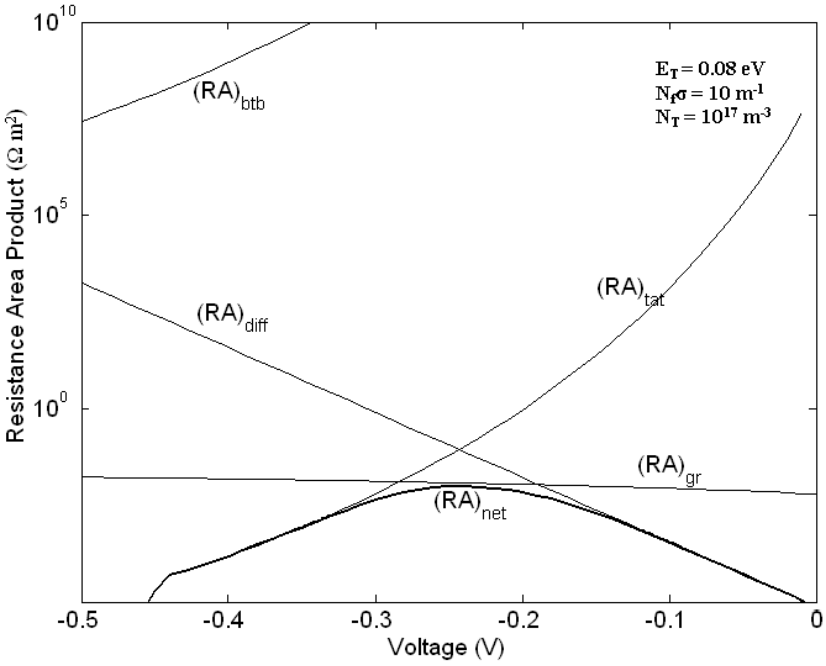

Fig. 4. Variation of different components of Resistance-Area (RA) product with applied reverse voltage.

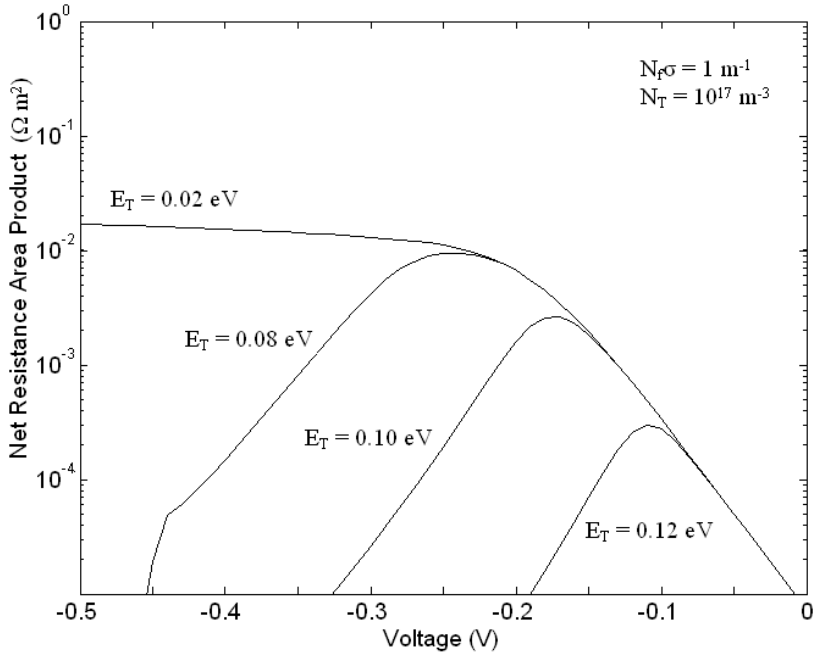

Fig. 5. Variation of total RA product with voltage for different values of E_T.

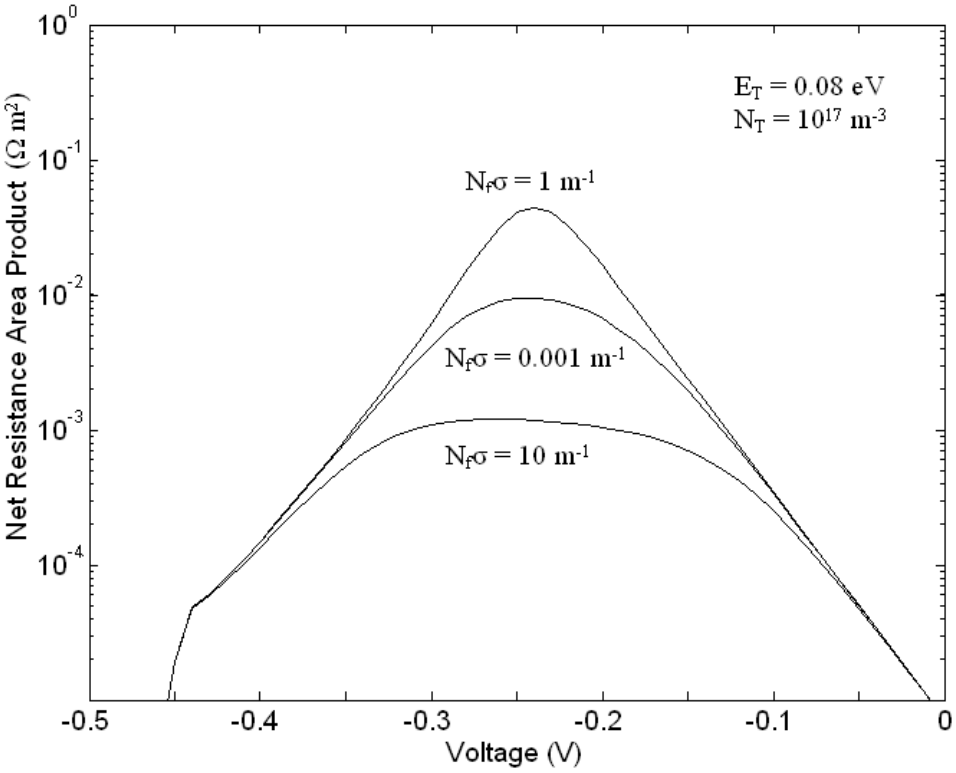

Fig.6. Variation of total RA product with applied voltage.

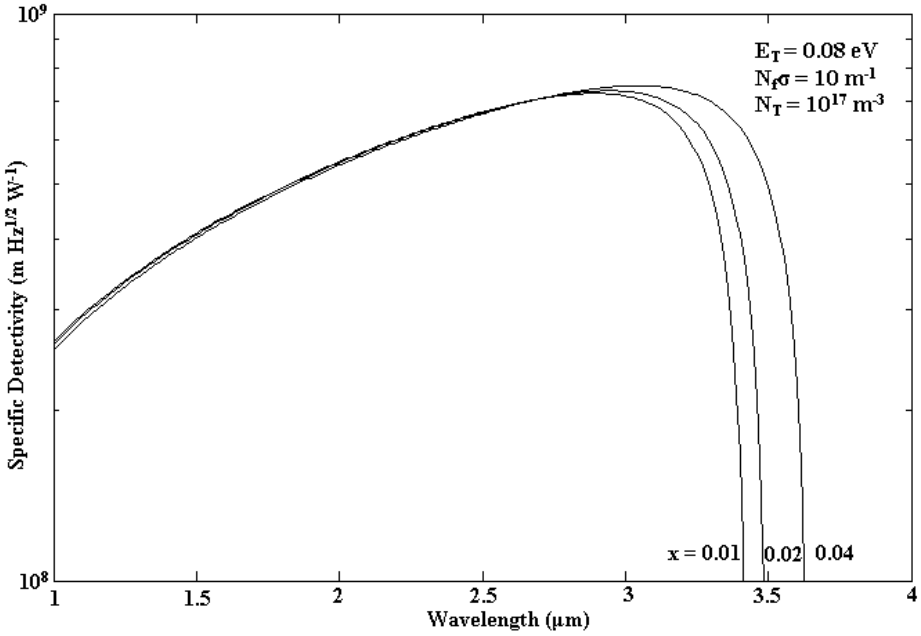

Fig.7. Variation of detectivity with wavelength for different material composition.